CrossMark

ORIGINAL

Modeling of mass and charge transport in a solid oxide fuel cell anode structure by a 3D lattice Boltzmann approach

Hedvig Paradis[1] · Martin Andersson[1] · Bengt Sundén[1]

Abstract A 3D model at microscale by the lattice Boltzmann method (LBM) is proposed for part of an anode of a solid oxide fuel cell (SOFC) to analyze the interaction between the transport and reaction processes and structural parameters. The equations of charge, momentum, heat and mass transport are simulated in the model. The modeling geometry is created with randomly placed spheres to resemble the part of the anode structure close to the electrolyte. The electrochemical reaction processes are captured at specific sites where spheres representing Ni and YSZ materials are present with void space. This work focuses on analyzing the effect of structural parameters such as porosity, and percentage of active reaction sites on the ionic current density and concentration of H_2 using LBM. It is shown that LBM can be used to simulate an SOFC anode at microscale and evaluate the effect of structural parameters on the transport processes to improve the performance of the SOFC anode. It was found that increasing the porosity from 30 to 50 % decreased the ionic current density due to a reduction in the number of reaction sites. Also the consumption of H_2 decreased with increasing porosity. When the percentage of active reaction sites was increased while the porosity was kept constant, the ionic current density increased. However, the H_2 concentration was slightly reduced when the percentage of active reaction sites was increased. The gas flow tortuosity decreased with increasing porosity.

✉ Hedvig Paradis
hedvig.paradis@energy.lth.se

Bengt Sundén
bengt.sunden@energy.lth.se

[1] Department of Energy Sciences, Faculty of Engineering, Lund University, Box 118, 221 00 Lund, Sweden

List of symbols

AV	Surface area to volume (m²/m³)
b	Particle distribution function, ion/electron transport
C	Concentration (mol/m³)
D_e	Effective diffusivity (m²/s)
D_{eff}	Average effective diffusivity (m²/s)
D_{Keff}	Effective Knudsen diffusivity (m²/s)
d_p	Particle diameter (m)
e	Base velocity in the lattice Boltzmann model
E	Activation energy (kJ/mol)
E	Actual voltage (V)
E^{eq}	Equilibrium voltage (V)
f	Particle distribution function, momentum transport
F	Faraday's constant (96,485 A s/mol)
g	Particle distribution function, mass transport
h	Particle distribution function, heat transport
i	Current density (A/m²)
L	Porous domain length (m)
M	Molecular weight (g/mol)
p	Pressure (atm)
Q	Heat flow (J/s)
R	Gas constant [8.3145 J/(mol K)]
Re	Reynolds number (–)
R_j	Reaction rate (mol/s)
S	Entropy (J/mol K)
T	Temperature (K)
t	Time (s)
u	Velocity vector (m/s)
u, v	Velocity (m/s)
x, y, z	Position (m)

Greek symbols

α	Lattice direction (–)
β	Transfer coefficient in the Butler–Volmer equation (–)

ε	Porosity (–)
η	Polarization (V)
ρ	Density (kg/m^3)
σ	Conductivity (S/m) or characteristic length (Å)
τ	Relaxation time (–)
ν	Kinematic viscosity (m^2/s)
ϕ	Electric potential (V)
Ω	Collision operator (–)
Ω_D	Dimensionless collision integral (–)

Abbreviations

BGK	Bhatnagar, Gross, Krook (method, collision operator)
CFD	Computational fluid dynamics
FEM	Finite element method
FDM	Finite difference method
FIB	Focused ion beam
FVM	Finite volume method
LBM	Lattice Boltzmann method
PDF	Particle distribution function
SEM	Scanning electron microscopy
SOFC	Solid oxide fuel cell
TPB	Three-phase boundary
YSZ	Yttria-stabilized zirconia

Chemical formula

H_2	Hydrogen
H_2O	Water
Ni	Nickel
O_2	Oxygen
O^{2-}	Oxygen ions

Subscripts

act	Activation
conc	Concentration
e	Electronic, electrochemical
io	Ionic
j	Species index
k	Species index
ohm	Ohmic
r	Reaction

1 Introduction

Solid oxide fuel cells (SOFCs), which are the subject of this study, offer a number of advantages for sustainable and efficient electricity generation, such as high conversion efficiency, high-quality exhaust heat and flexible fuel input [1]. If the performance is improved and the cost is decreased, SOFC can stand as a viable sustainable power generating device for a broad range of applications from mobile phones to power stations. SOFCs are interesting

for two main reasons as a power generating device. Firstly, they can convert fuel to electricity directly without any mechanically moving parts and are therefore highly efficient as power generating devices. Secondly, they can function with a variety of different fuels due to their high operating temperature (600–1100 °C) [1].

SOFCs with a supportive anode structure is usually built up by nickel/yttria stabilized zirconia (Ni/YSZ) cermet with high electrochemical performance and good chemical stability [1, 2]. The porous anode plays an important role in this type of configuration, both as a main actor for the active transport processes and as a support for the cell. The performance of an SOFC depends on many parameters but among the critical ones are the functionality of the porous anode microstructure, kinetics and availability of active reaction sites. The materials have become increasingly sophisticated in structure and composition. For the purpose of computational modeling of SOFCs, the transport processes within the anode must be captured at the microscopic scale, and their role included in macroscale physical processes. There is a need for a better understanding of the details of the microscopic physical processes in the porous structure of the anode with the reaction sites. In order to be able to explore the complexities of the SOFC, it is important to model the physical processes on their correct length and time scales, and to combine the information from the different scales in a numerical model.

The microstructure presented in the macroscale models are basically described by a few empirical parameters (e.g., porosity and tortuosity). Not only are these parameters difficult to measure but they cannot properly describe the microscopic physical behavior [3, 4]. These parameters are obtained through experimental studies or detailed numerical studies of the microscopic material and can often only be described three-dimensionally. With this said, microscale modeling for the porous electrodes with the electrochemical and chemical reactions is essential for the progress of fuel cells. Functional electrode structures are known to work in favor of electrochemical reactions, reforming reactions and transport processes [5, 6]. In the real SOFC porous samples, the structures are highly distributed and the active TPB density may vary considerably within the porous sample [3]. However, these porous structures are hard to regenerate in a computational model. In this study, the geometry is built up by homogeneous spherical particles and randomly placed reactive sites where a three-phase-boundary (TPB) exists.

A considerable amount of research has been conducted on SOFCs to date, and the various computational methods used vary from macroscale to nanoscale, as discussed in the previous section. Some studies on the interaction of charge and mass transport with chemical and electrochemical reactions will be discussed below. The effects of electrode

microstructure on activation and concentration polarization (losses) in SOFCs have been studied by Virkar et al. [7] considering only a steady-state, one-dimensional model for gas diffusion. It was shown that polarization losses can be minimized by optimization of the electrode micro structure. Detailed multi-dimensional modeling of the transport processes inside fuel cells is very useful in design and research studies.

Suzue et al. [8] reconstructed the porous media of an SOFC anode by a stochastic model to evaluate the structural parameters and developed a 3D model by LBM to analyze the charge and mass transport of the SOFC anode. It was concluded that when the temperature was increased, the reaction zone in the anode became thinner and the current concentration appeared closer to the electrolyte interface. Iwai et al. [9] also reconstructed the anode of an SOFC by the Focused Ion Beam Scanning Electron Microscopy (FIB-SEM) method and developed a 3D LBM model to evaluate the mass and charge transport. Iwai et al. [9] focused on quantification of microstructural parameters such as tortuosity, TPB length and volume fraction by two different methods. It was concluded that the methods only differed by less than 3 %. Kanno et al. [10] also reconstructed the porous anode of an SOFC by FIB-SEM. The reconstructed anode was used as the geometry of a 3D LBM model to analyze the charge and mass transport to evaluate the losses of the anode. It was concluded that a smaller sample of the reconstructed porous media led to an under-prediction of the overpotential.

Several previous studies have been conducted on SOFC. However, there exist a limited number of studies analyzing the performance of the SOFC anode at microscale with the momentum, charge, heat and mass transport processes coupled. In this study all these transport processes are coupled and the equations for these processes are solved simultaneously. The aim of this study is to determine the interaction between the transport and reaction processes in the anode of an SOFC through simulations carried out using LBM. The microscale model simulates charge, momentum, heat and mass transport with electrochemical reactions in the porous anode structure of an SOFC in 3D for a geometry built up with randomly placed spheres as a replica of a porous anode. The modeling domain includes specific active reaction sites where all three phases of Ni, YSZ and void space are present. The use of homogeneous spheres for building the model geometry is chosen to more easily control the porosity and the number of specific reaction sites. The focus is on the effect of structural parameters such as porosity and percentage of reaction sites on the ionic current density and concentration of H_2. Some of the inlet and boundary conditions for the microscale model are obtained from our previous macroscale model [1]. This

is a first step towards coupling the microscale model in this study with the previously developed macroscale model.

2 Governing equations

There are two general electrochemical reactions if the fuel cell is fed with hydrogen and the reactions are handled in a global scheme manner. The active species involved in this case are hydrogen and oxygen. The species reactive transport is initiated with a hydrogen (H_2) molecule diffusing through the pores in the anode combined with a negatively charged oxygen ion (O^{2-}) traveling through the solid electrolyte from the cathode side. H_2 forms a molecule of H_2O during this oxidation reaction and releases a pair of electrons. The H_2O molecule formed at the TPB then diffuses back through the pores in the anode while the electrons generated at the anode TPB are conducted through the anode material to the current collector, and finally flow through an external circuit. The electrons enter the cathode and are conducted through the cathode material to the cathode TPB. Here, the electrons combine with oxygen that has diffused from the air through pores in the cathode to create oxygen ions as indicated in Eq. (2). These ions are conducted through the electrolyte and the cycle is completed [2, 6].

$$H_2 + O^{2-} \rightarrow H_2O + 2e^- \qquad (1)$$

$$\frac{1}{2}O_2 + 2e^- \rightarrow O^{2-} \qquad (2)$$
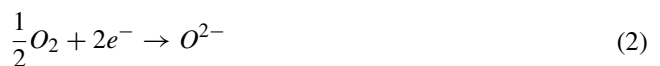
Note that only Eq. (1) is modeled in this study. Both Eqs. (1) and (2) provide the needed reactions for the SOFCs functionality with H_2 as fuel and the closed loop for the transport of the electrons.

The physical processes for the modeling domain are represented by four main equations in this study. First, the reaction–advection–diffusion equation can be written in general form as [11, 12]:

$$\frac{\partial C_j}{\partial t} + (\boldsymbol{u} \cdot \nabla)C_j - D_{jk}\nabla^2 C_j = R_j \qquad (3)$$

where C_j is the concentration of species j, D_{jk} is the diffusion coefficient between the two species j and k, R_j the reaction rate for reaction with the specific species j, $\boldsymbol{u}$ the velocity vector and t is time. The electrochemical reactions are implemented by source terms as:

$$R_{H_2} = \frac{-i}{2 \cdot \mathrm{F}} \qquad (4)$$

$$R_{H_2O} = \frac{i}{2 \cdot \mathrm{F}} \qquad (5)$$

where i is the current density and F the Faraday constant. Second, the Navier–Stokes equations for conservation of momentum and the conservation of mass are presented as:

$$\frac{\partial \boldsymbol{u}}{\partial t} + (\boldsymbol{u} \cdot \nabla)\boldsymbol{u} + \Delta p - \upsilon \nabla^2 \boldsymbol{u} = 0 \tag{6}$$

$$\nabla \cdot \boldsymbol{u} = 0 \tag{7}$$

where p is the pressure for the fluid and ν is the kinematic viscosity. The third equation concerns heat transfer and is presented below in terms of temperature.

$$\frac{\partial T}{\partial t} + (\boldsymbol{u} \cdot \nabla)T - \alpha \nabla^2 T = Q \tag{8}$$

where T is the temperature, α the thermal diffusivity and Q the heat flux. The heat flux is based on heat generation by the electrochemical reactions and on the losses through the activation, the concentration and the ohmic polarizations,

$$Q = i \cdot \left(\frac{T \cdot \Delta S_r}{n_e \cdot F} + \eta_{act} + \eta_{conc} \right) + \sum \frac{i^2}{\sigma} \tag{9}$$

where ΔS_r is the entropy change of the reaction (−50.2 J/(K mol) [1, 13, 14]) and σ the ionic or electronic conductivity. Whereas the above mentioned equations represent the transport processes, the fourth and fifth equations are the charge transport in terms of the electronic and ionic potential. The ion and electron transport is presented as [3, 10, 15]:

$$\sigma_{io} \nabla^2 \phi_{io} = i_{io} \cdot AV_e \tag{10}$$

$$\sigma_e \nabla^2 \phi_e = -i_e \frac{i^2}{\sigma} AV_e \tag{11}$$

where σ is the ionic or electronic conductivity, ϕ the ionic or electronic potential and AV_e the surface area to volume for the electrochemical reaction. The subscripts io and e represents ionic and electronic, respectively. The influence of different potentials/polarizations varies depending on cell operating conditions and design/structure. The local potentials vary between different positions (in 3D) within the cell and they are affected by, for example, the local hydrogen and oxygen concentrations, the local temperature as well as the ion and electron transport path.

Further, the following equations below are described to clarify a number of parameters in the main equations in the 3D model. The current density can be obtained through the Butler–Volmer equation [2, 4, 15]. If the transfer coefficient is assumed to be 0.5, the Butler–Volmer equation is reduced to Eq. (12) which is based on the assumption of symmetric electron transfer in the Butler–Volmer equation and the activation overpotential is mainly important

at small currents. This often agrees well with experimental Tafel plots [15].

$$i = 2 \cdot i_0 \cdot sinh\left(\frac{n_e \cdot F \cdot \eta_{act}}{2 \cdot R \cdot T} \right) \tag{12}$$

$$\eta_{act} = \phi_e - \phi_i - E_{eq} \tag{13}$$

$$i_0 = \frac{R \cdot T}{n_e \cdot F} \cdot k_e'' \cdot exp\left(\frac{-E}{R \cdot T} \right) \tag{14}$$

$$E^{OCV} = E_0 - \frac{R \cdot T}{2F} ln\left(\frac{p_{H2O}}{p_{H_2} \cdot (p_{O_2})^{0.5}} \right) \tag{15}$$

$$\eta_{conc} = \frac{R \cdot T}{n_e \cdot F} ln\left(\frac{p_{H_2,TPB} \cdot p_{H_2O,b}}{p_{H_2,b} \cdot p_{H_2O,TPB}} \right) \tag{16}$$

where k_e'' the pre-exponential factor which is $6.54 \times 10^{11} \, \Omega^{-1} \, m^{-2}$ [13], i_0 the exchange current density, n_e the number of electrons transferred per reaction, $\eta_{act,e}$ the electrode activation polarization over-potential, R the ideal gas constant, E^{eq} the equilibrium voltage, E the activation energy (140 kJ/mol [13]), and p is the partial pressure for the H_2 and H_2O at the TPB or b (bulk fluid). Note that E_0 is the theoretical voltage. Equation (16) is valid for equilibrium conditions. If the detailed charge transfer carriers and pathways are neglected, the overpotential at the TPB sites can be held constant. Due to internal resistance and polarizations (overpotential losses), the actual voltage (E) becomes less than the open-circuit voltage. The actual voltage can be expressed as:

$$E = E^{OCV} - \eta_{act} - \eta_{ohm} - \eta_{conc} \tag{17}$$

where η is the polarization due to activation, concentration and ohmic losses, respectively.

In this study, an averaged effective diffusivity is used to take into account both the ordinary and Knudsen diffusivity. The mass transport at the microscale range is analyzed for the diffusion within the SOFC anode and the Knudsen diffusion is considered in the calculations. Including the Knudsen diffusion for SOFCs is commonly done in the literature, see [5, 7, 8, 10, 13].

The effective diffusivity by Knudsen diffusion is defined as [16, 17]:

$$D_{Keff} = \frac{d_p}{3} \cdot \sqrt{\frac{8 \cdot R \cdot T}{\pi \cdot M_{jk}}} \tag{18}$$

where d_p is the particle diameter and M_{jk} is the average molecular weight of species j and k defined as [16, 17]:

$$M_{jk} = 2 \cdot \left[\frac{1}{M_j} + \frac{1}{M_k} \right]^{-1} \tag{19}$$

The effective diffusivity which is based on the ordinary diffusion is defined here as [16, 17]:

$$D_e = \frac{0.0026 \cdot T^{3/2}}{P \cdot M_{jk}^{1/2} \cdot \sigma_{jk}^2 \cdot \Omega_D} \qquad (20)$$

where, besides the parameters mentioned above which remain the same, σ_{jk} is the characteristic length between the colliding molecules which depends on the choice of the intermolecular force law and Ω_D the dimensionless collision integral. Note that the pressure P is 1 bar in Eq. (20) and that the parameters in this equation are not all in SI units. The ones which differ from the SI unit standard are M_{jk} (g/mol) and σ_{jk} (Å). The effective diffusivities are then averaged as below [16, 17]:

$$D_{eff} = 2 \cdot \left[\frac{1}{D_{Keff}} + \frac{1}{D_e} \right]^{-1} \qquad (21)$$

3 Lattice Boltzmann modeling

LBM is based on the Boltzmann equation and is perceived as an alternative to the traditional CFD based on the Navier–Stokes equation. LBM keeps track of the movements of molecule ensembles and the evolution of the distribution functions and recovers the different transport equations by recovering the macroscopic parameters. LBM has shown promising simulation results of fluid flows and mass diffusion through complex geometries. Conventional CFD methods use fluid density, velocity and pressure as the primary variables, while the LBM uses a more fundamental approach with the so-called particle velocity distribution function (PDF) [18–20]. Despite LBM's simplicity, it has a disadvantage of taking up more memory than a traditional CFD approach. For this case parallel computing offers the opportunity to include several physical processes in the model with success. LBM is comparable to conventional methods such as Finite Element Method (FEM), Finite Volume Method (FVM) and Finite Difference Method (FDM) in terms of functionality, accuracy and computational time for physical problems, especially on component level or at microscale. Some of the main advantages of LBM over the conventional methods are computational efficiency and easy implementation of parallelization. Also LBM offers the ability to handle a geometry as complex as desired, because the method does not need to create a volume mesh while the conventional methods need to generate a volume mesh and may fail when the geometry becomes too complex. Kandhai et al. [21] and also Geller et al. [22] have conducted comparative studies on LBM with FEM and FVM on mixer reactors and laminar flows, respectively. LBM has also been used as a numerical method for transport processes in SOFCs and it has been compared with conventional methods such as FDM, FEM and FVM [20].

LBM's main function, PDF, is defined as the number of particles of the same species travelling along a particular direction with a particular velocity. LBM is built up on lattice points which are given locations placed all over the regularized solution domain. The LBM is described by two different actions taking part at each lattice point (site); namely streaming and collision [18, 19]. Streaming describes the movement of the particles of each species and collision describes interactions between the particles of the same or different species. In this study, the number of directions is 19 for the PDF which recovers the conservation of momentum and mass. To recover the other equations the number of directions is 7. The theory shows it is sufficient with 7 lattice directions to capture the phenomena for the continuum equations. For more information regarding the functionality of the scheme of D3Q7, the reader is referred to [23–25]. The collision operator used in all the particle distribution functions is the Bhatnagar, Gross and Krook (BGK) [26] collision operator which is the most simple collision operator in LBM. There are other possible choices besides the BGK, e.g., the Multi-Relaxation-Time. This is often chosen because it is numerically more stable but on the other hand the computations are slower. In this model, stability is not an issue mainly because the low Reynolds number of the flow. For BGK, it is assumed that the particle distribution function relaxes to an equilibrium state after the collision at a single relaxation time [26]. For small enough dt and dx and, small Mach numbers, it can be shown by the Chapman–Enskog expansion analysis that this numerical scheme solves the equation of an incompressible fluid flow at the limit of weak compressibility with second order accuracy. The method has been developed to handle more than the momentum transport. By applying the Chapman–Enskog expansion it is possible to derive a correct LB model for other physical processes such as heat or charge transport. LBM-BGK schemes similar to that for advection and diffusion have been used for a scalar field for example temperature (heat/enthalpy) by the LB community (Shan and Doolen [27]; Huber et al. [28]) or chemical transport processes (Kang et al. [29]). The PDF is combined by the streaming and collision in the LB equation and is here presented for species j [4, 18, 19, 30–32].

$$f_\alpha^j \left(x + e_\alpha^j \cdot t, t + \Delta t \right) = f_\alpha^j(x, t) + \Omega_\alpha^j(x, t) + F_\alpha^j(x, t) \quad (22)$$

where f_α^j is the PDF, e_α^j the velocity, Ω_α^j the collision term, Δt the simulation time step and F_α^j the source term at any spatial location x and time t along the direction α. The collision term and the equilibrium function are specified as:

$$\Omega_\alpha^j(x, t) = -\left(\frac{f_\alpha^j(x, t) - f_\alpha^{j,eq}(x, t)}{\tau_j} \right) \qquad (23)$$

$$f_\alpha^{j,eq} = w_\alpha \cdot C_j \left[1 + 3 \cdot e_\alpha \cdot u_j \right] \tag{24}$$

$$u_j = \frac{\sum_j \frac{1}{\tau_j} \cdot \sum_\alpha f_\alpha^j e_\alpha}{\sum_j \frac{1}{\tau_j} C_j} \tag{25}$$

where w_a is the weight factor due to the placement of the particles in the grid, u_j is the specific velocity contribution and τ_j is the relaxation time for the specific species j. When the mass diffusion is modeled in LBM, two approaches are often used; pure diffusion or advection–diffusion (also called convection–diffusion). Pure diffusion and advection–diffusion are simulated with different equilibrium distributions $f_{\sigma,\alpha}^{eq}$ The equilibrium distribution for advection diffusion is presented in Eq. (24) but for the case of pure diffusion $u = 0$ in Eq. (24). There is no need for a higher order of terms in the equilibrium distribution for the propagation of species. This can be obtained by Chapman–Enskog analysis on the advection–diffusion equation. The reader is referred to Latt [31] for detailed information. In this case for the simulation of mass transport, the force term includes the effect of the chemical reactions and is shown below [10, 27, 33]:

$$F_\alpha^j(x, t) = w_\alpha \cdot \Delta t \cdot R_j \tag{26}$$

where w_α is the weight function along the direction α, and R_j the reaction rate in lattice units for species j. Δt and Δx are the time step and length step in the simulation, respectively. These are defined in real units, (s) seconds and (m) meters, respectively. The concentration C is obtained directly in (mol/m^3) which has been shown by several authors [12, 19, 33, 34]. The concentration is obtained by Eq. (26) [12, 18, 19, 27].

$$C_j = \sum_{\alpha=0}^{6} f_\alpha^j(x, t) \tag{27}$$

To recover the equation for conservation of momentum, a PDF, named g_a, is applied as:

$$g_\alpha(x + \Delta x, t + \Delta t) = g_\alpha(x, t) + \Omega_{\alpha,g}(x, t) \tag{28}$$

$$\rho = \sum_{\alpha=0}^{18} g_\alpha \tag{29}$$

$$g_\alpha^{eq}(x) = w_\alpha \cdot \rho \left[1 + 3\frac{e_\alpha \cdot v}{c^2} + \frac{9}{2}\frac{(e_\alpha \cdot v)^2}{c^4} - \frac{3}{2}\frac{v^2}{c^2} \right] \tag{30}$$

$$v = \frac{1}{\rho} \cdot \sum_{\alpha=0}^{18} g_\alpha e_\alpha \tag{31}$$

where g_α is the PDF for momentum, e_α the velocity, Ω_α the collision term, ρ is the density of the fluid and v the fluid velocity. Two different PDFs are used to recover the ion and electron transport. For simplicity and due to similarities between the equations, it is only written out here once. The ion or electron transport uses a PDF, named b_a, which is applied as [34]:

$$b_\alpha(x + \Delta x, t + \Delta t) = b_\alpha(x, t) + \Omega_{\alpha,h}(x, t) + B_\alpha(x, t) \tag{32}$$

$$B_\alpha(x, t) = w_\alpha \cdot \Delta t \cdot i \tag{33}$$

$$b_\alpha^{j,eq} = w_\alpha \cdot \phi_j \left[1 + 3 \cdot e_\alpha \cdot u_j \right] \tag{34}$$

$$\phi = \sum_{\alpha=0}^{6} b_\alpha \tag{35}$$

where b_α is the PDF for ionic or electronic potential, B_α the source term at any spatial location x and time t along the direction α and ϕ the ionic or electronic potential depending on which equation being simulated. A BGK collision operator is used for the PDF recovering of the ion/electron transport. In a similar manner as for the mass diffusion, a particle distribution function is set up for the temperature [27, 28]:

$$h_\alpha(x + \Delta x, t + \Delta t) = h_\alpha(x, t) + \Omega_{\alpha,h}(x, t) + H_\alpha(x, t) \tag{36}$$

$$H_\alpha(x, t) = w_\alpha \cdot \Delta t \cdot Q \tag{37}$$

$$h_\alpha^{j,eq} = w_\alpha \cdot T_j \left[1 + 3 \cdot e_\alpha \cdot u_j \right] \tag{38}$$

$$T = \sum_{\alpha=0}^{6} h_\alpha \tag{39}$$

where h_α is the PDF for temperature, H_α the source term for the heat transport equation at any spatial location x and time t along the direction and T the temperature. Q is defined in Eq. (9). A BGK collision operator is used for the PDF recovering the heat transport. The temperature is not explicitly illustrated in the results of this article because it is in general rather constant with a temperature difference of only 5 K along the main flow direction (x-direction) in this study.

The relation between the SI units and the lattice units is formed by using the parameters Δx and Δt, which are the discrete space step and time step, respectively [31]. The relation is handled through the equations given below:

$$\Delta x = \frac{L_P}{N} \tag{40}$$

$$\Delta t_{fluid} = \frac{\upsilon_{LB}}{\upsilon_P} \cdot \Delta x^2 \tag{41}$$

Table 1 Parameters in the SOFC analysis

Parameter	Value
Cell length	150 µm
Anode thickness and height	75 µm
Particle diameter	0.25–1 µm
Porosity	0.3–0.5
Diffusivity D_{H2H2O} [35]	4×10^{-5} m²/s
Viscosity [1]	2.5×10^{-4} m²/s
Ionic conductivity [10]	$3.34 \times 10^4 \cdot \exp(-10{,}300/T)$ S/m
Electronic conductivity [10]	$3.27 \times 10^6 - 1065.3 \cdot T$ S/m

Table 2 Inlet and operating conditions [1]

Parameter	Value
Inlet concentration of H_2 ($x = L$)	10 mol/m³
Inlet concentration of H_2O ($x = 0$)	1 mol/m³
Inlet velocity v_x ($x = 0$)	0.015 m/s
Inlet temperature ($x = 0$)	950, 1000, 1050 K
Outlet Pressure ($x = L$)	1 atm

$$v_{LB} = \frac{1}{3} \cdot \left(\tau_{fluid} - 0.5 \right) \qquad (42)$$

where L_p is the physical length in one length direction and N the number of grid points in the same length direction. Further, v is the kinematic viscosity in physical units and v_{LB} is the lattice Boltzmann viscosity. τ is the relaxation time and is usually set to a value around 1 [31].

In a similar manner this can be done for the species, potential and temperature. Here it is only shown for the temperature and H_2:

$$\Delta t_T = \frac{\alpha_{LB}}{\alpha_P} \cdot \Delta x^2 \qquad (43)$$

$$\alpha_{LB} = \frac{1}{3} \cdot (\tau_T - 0.5) \qquad (44)$$

$$\Delta t_{H2} = \frac{D_{H2}}{\Delta x^2} \cdot \Delta t_T \qquad (45)$$

where α is the thermal diffusivity in SI units and α_{LB} is the lattice Boltzmann thermal diffusivity based on the thermal relaxation time [31].

The values of the boundary conditions for the LB model are extracted from a previously developed FEM model [1, 35] namely inlet velocity, interface conditions for the potential distributions and inlet concentration for the gas species. The parameters concerning the cell structure and transport processes for the calculations are presented in Table 1 and the inlet and operating conditions are presented

in Table 2. The boundary condition at $x = L$ is specified for the concentration of H_2 and at $x = 0$ the mole flux is specified for the H_2. For the planes at $y = 0$ and at $y = L$ as well as $z = 0$ and at $z = H$ periodic boundary conditions are used. A small amount of water is set as an inlet condition ($x = 0$) to enable the transport and reaction processes. Note that L and H are length and height dimension constants, respectively. The reactions are implemented at the anode/electrolyte interface and at specific reaction sites. In this study the x-direction is along the main flow direction, whereas the y-direction is perpendicular to the main flow direction. Initially, the velocity in the x-direction is set to a constant value of 0.015 m/s and set to zero in the y- and z-directions to replica the situation for the transport processes in a whole SOFC as in the macroscale model. The electronic potential is set to zero at $x = 0$, specified as a constant value at $x = L$ and all other boundaries are set to be periodic. The ionic potential is set to zero at $x = L$, specified to a constant value at $x = 0$ and all other boundaries are set as periodic. The boundary condition for the temperature at $x = 0$ is set as a constant value and the outlet is defined as a convective flux boundary condition. All other boundaries for the temperature distribution are specified as periodic boundary conditions.

To treat the electrode structure realistically, there will be obstacles treated like impermeable solid surfaces for the gas species [12, 31]. The obstacles are suited for no-slip reflection which is simply a bounce-back definition where the particles are reflected back in the same direction as they arrived. However, the ions and electrons will travel through the solid particles in the porous domain.

The tortuosity is also calculated in during the simulation as it is an important parameter in macroscale models for SOFCs. A common definition of the tortuosity, which is used in this study, is the ratio of the length of the actual path of the fluid particles to the shortest path length in the direction of the flow [36]. However, the definition of tortuosity may vary; in some models it represents the effect of additional pathways, while in others it is simply a numerical parameter adjusted to fit the experimental data [36]. It should also be mentioned that the tortuosity differs for gas-phase transport and ion and electron transport. The tracking of the fluid particles is one of the main features of the LBM, which makes it fairly easy to obtain the tortuosity based on the streamlines or velocity field when the transport processes are simulated. However, the value of the tortuosity obtained is specific to the porous medium considered in the simulation, and will be different for other porous media.

Some of the physical parameters are taken from our previously developed macroscale two-dimensional CFD model covering an intermediate temperature anode-supported SOFC [1, 35]. The significant parameters concerning the
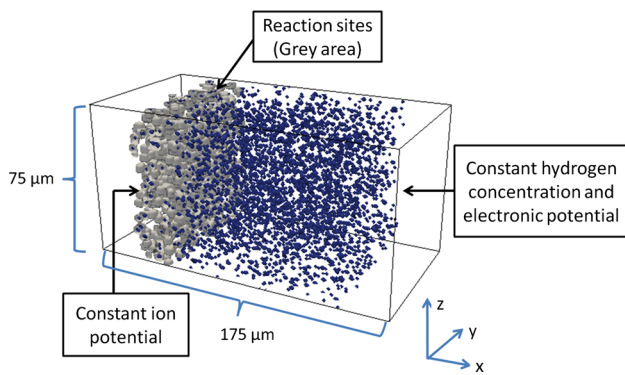
Fig. 1 Schematic figure of the modeling domain with descriptive boundary conditions and size of the domain

Fig. 2 Velocity distribution (m/s) in the modeled porous domain

Fig. 3 Concentration distribution of H_2 (mol/m^3)

cell structure and transport processes for the calculations are presented in Table 1 and the inlet and operating conditions are presented in Table 2.

To visualize the flow in the complex geometry, the 3D porous domain is created through randomly placed spherical obstacles which can be viewed in Fig. 1. In Fig. 1 the modeling geometry is presented with placement of the boundary conditions and the size of the modeling domain. The space before the inlet represents an electrolyte interface and the outlet without any spheres is used to check the flow for an undisturbed domain. The modeling domain in this study represents only a small part of the anode close to the electrolyte to capture the electrochemical activity. The modeling geometry consists of specific active reaction sites throughout the domain. These specific sites are simulated to represent the TPB locations. There are two different sizes of the spherical particles to represent Ni and YSZ. When one Ni and one YSZ sphere, that is to say one sphere of each size, are close enough to each other and connected with a pore space, an active reaction site is created. Note that the two different sizes of spheres are not connected specifically to the phases Ni or YSZ but are used to identify the active sites where one sphere of each size is needed. The ions and electrons will travel through the solid particles and will not be specifically connected to YSZ or Ni. Both ions and electrons are able to travel through both types of spheres. In Fig. 1, the blue randomly placed spheres of two different sizes represent the particles of Ni and YSZ. A grey coverage is placed on top of the blue spheres to visualize where the reactions take place. The grey coverage in Fig. 1 represents a coating to illustrate that the reactions only take place on the surface of the particles where the active site is located. Note that Fig. 1 is not to scale in size and porosity but is just presented to visualize the geometry and the placement of the reaction sites.

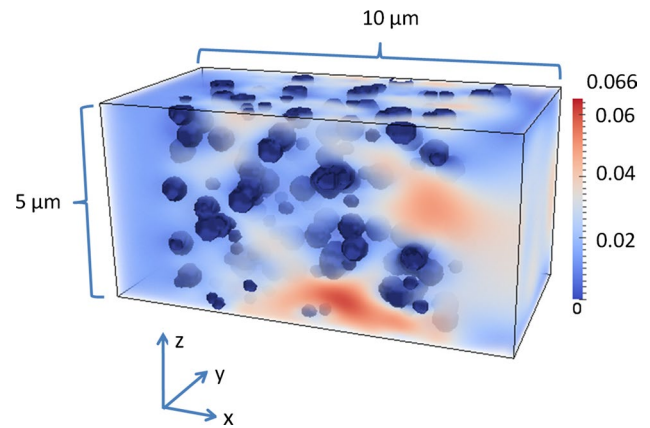Reynolds number (*Re*) varies throughout the modeling domain as it is a porous media. In this study, throughout the porous domain, the Reynolds number is Re $\leq$ 0.01. The inlet velocity of 0.015 m/s leads to Re $\approx 5 \times 10^{-5}$ based on the pore diameter. The average velocity is extracted from our previous macroscale model in COMSOL Multiphysics [1, 35]. The production and consumption of species are included by implementing the reaction rate of the electrochemical reaction, shown in Eq. (3), in the mass diffusion equation.
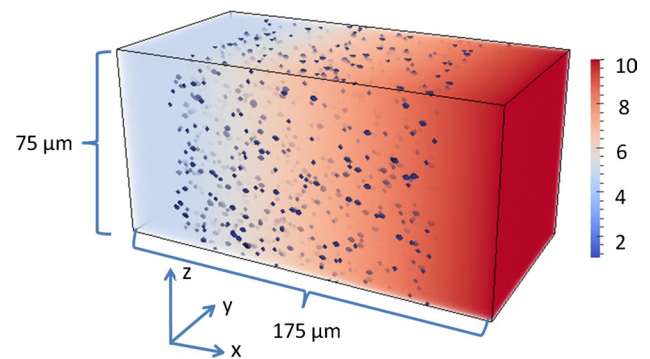
4 Results and evaluation

For the simulations, a computer cluster provided by Lunarc at Lund University is used. The modeling studies are performed in Palabos and part of it in MATLAB to compare the standard of the in-house codes to a commercial program.

In Fig. 2, the velocity field is presented to illustrate that LBM can easily handle the obstacles in a porous domain by the bounce-back effect for the particles at the obstacle wall. The velocity distribution is presented for part of the modeling domain with the enlarged particles (dark blue)
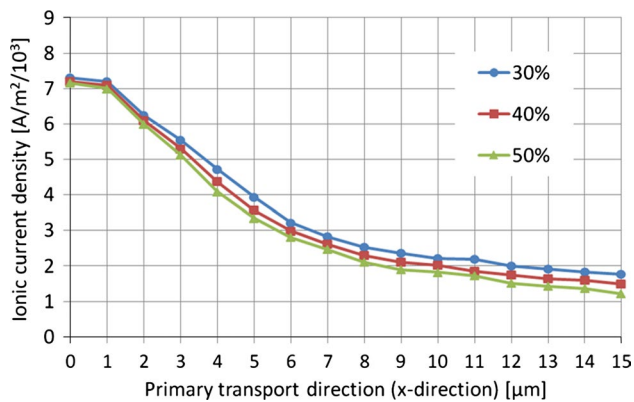
Fig. 4 Ionic current density along the center of the modeling domain for porosities of 30, 40 and 50 %, respectively

Fig. 5 Concentration distribution of H_2 along the center of the domain for porosities of 30, 40 and 50 %, respectively

to provide an understanding of the bounce-back theory which most easily is viewed for the fluid flow process in the porous media. The velocity in the porous domain is low and it is fully laminar throughout the whole model. As seen in Fig. 2, the local velocity is increased when the passages between the particles are narrow and the local velocity is decreased when the passages are broad.

Figure 3 shows the concentration distribution of H_2 for the porous domain with spherical obstacles of the entire modeling domain. The inlet concentration is specified at $x = L$ as 10 mol/m^3 (which can be converted into a mole fraction of $x_{H_2} = 0.9$) and the concentration flux is specified to zero at $x = 0$ normal to the boundary interface in the flow direction. The mass diffusion of H_2 predicts a continuous reduction of H_2 in the opposite flow direction. H_2O increases throughout the modeling domain from $x = 0$ to $x = L$.

Figure 4 presents the ionic current density distribution at the center of the porous modeling domain along the main flow direction. The ionic current densities are plotted for cases with different porosities ranging from 30 to 50 %. Note that the ionic current density is only plotted for the region closest to the electrolyte from 0 to 15 µm. Most activity occurs at the interface to the electrolyte and the anode structure has an active reaction zone of about 15 µm. The ionic current density decreases along the main flow direction. The decreased ionic current density (along the main flow direction) can be explained by an increased temperature and a decreased concentration of the electrochemical reactants. An increase in porosity decreases the ionic current density slightly. In contrast to the effect of temperature, the difference in magnitude between the ionic current density lines for various porosity is larger closer to $x = L$ which can be explained as an effect of the number of reaction sites and because the reacting species decreases as the porosity increases. The percentage of reaction sites
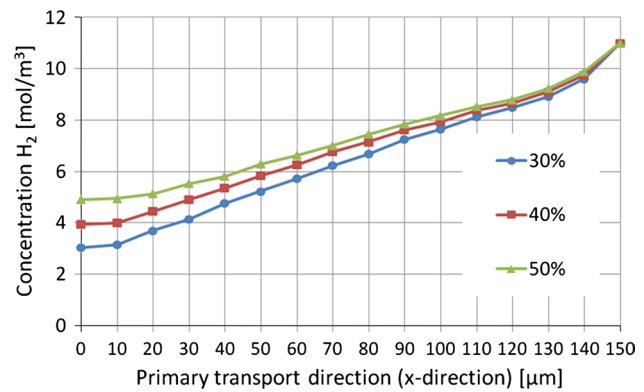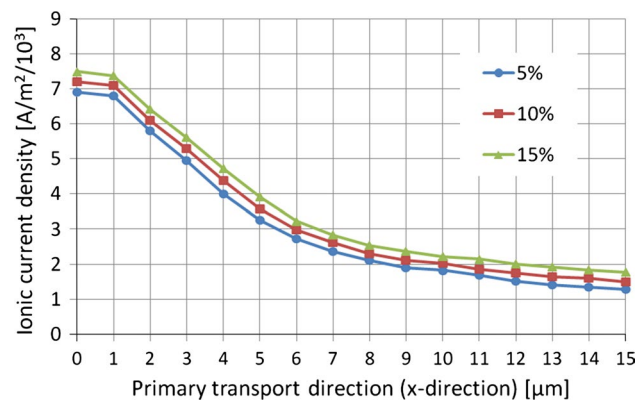

Fig. 6 Ionic current density along the center of the domain for three different percentages of reaction sites: 5, 10 and 15 %

remains the same but the number of particles decreases which decreases the number of reaction sites. The decrease in ionic current density along the main flow direction can be explained due to the influence of the charge transfer losses, η_{ohm}, depends mostly on the ion conductivity. Higher current density due to less available concentration of the reacting species will decrease the open-circuit voltage (along the main flow direction).

Figure 5 presents the concentration distribution of H_2 along the center of the porous modeling domain along the main flow direction, for the three porosities studied. The percentage of active reaction sites was 10 %. The H_2 concentration distributions were similar for all porosities. As the porosity increases the H_2 consumption decreases, and is more visible towards $x = 0$, as most of the H_2 is consumed. This can be explained by the fact that less reaction sites are available as there is more pore space between the solid particles. The H_2 consumption will also decrease with increasing porosity, as fewer active reaction sites come into contact with the gas species. If the porosity is decreased to
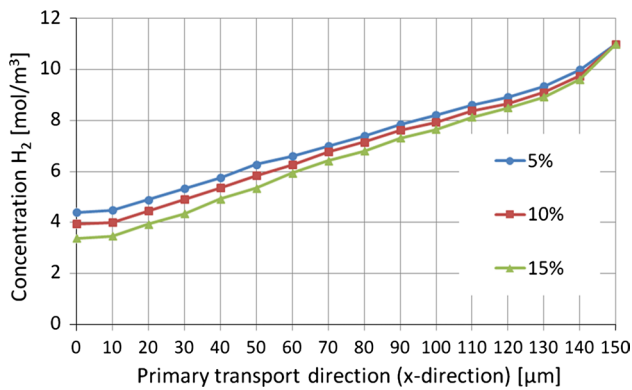
Fig. 7 Concentration distribution of H_2 along the center of the domain for different percentages of reaction sites of 5, 10 and 15 %, respectively

Fig. 8 Tortuosity in the anode for porosities of 30, 40 and 50 %, using three random reconstructions of the porous medium

the point where the fluid flow pathways are compressed, the H_2O production will decrease rapidly.

Figure 6 shows the ionic current density distribution at the center of the porous modeling domain from $x = 0$ to $x = 15$ μm, with percentages of active sites ranging from 5 to 15 %. Note that the specific active reaction sites are described by the volume percentage of the total volume of the particles. The reaction layer is assumed to be located at the anode–electrolyte interface. The ionic current density decreases rapidly with distance from the inlet, which indicates resistance by diffusion. Decreasing the percentage of active sites decreases the ionic current density slightly along the flow direction. Values of active sites greater than 15 % were also simulated, but the increase in ionic current density was less significant above 20 %, where it appears that less reacting species are available. In future studies it might be of interest to investigate the effect on the transport processes and current density by gradients in the percentage of active sites, by linearly decreasing the number of active sites starting from the electrolyte boundary.

Figure 7 presents the concentration distribution of H_2 at the center of the porous modeling domain from $x = 0$ to $x = 150$ μm, as a function of the percentage of reaction sites. The porosity was kept constant at 40 %, as well as the number of particles. It can be seen that the concentration distributions of H_2 are similar in all cases. However, as the percentage of reaction sites increases, the H_2 consumption increases. This is more visible towards $x = 0$ as most of the H_2 has been consumed.

The tortuosity was evaluated by measuring the lengths of all the streamlines, and calculating the average length divided by the length of the cell. The values of different tortuosities for the gas species are presented in Fig. 8. Three cases were studied for each porosity using different randomly placed spheres throughout the modeling domain.
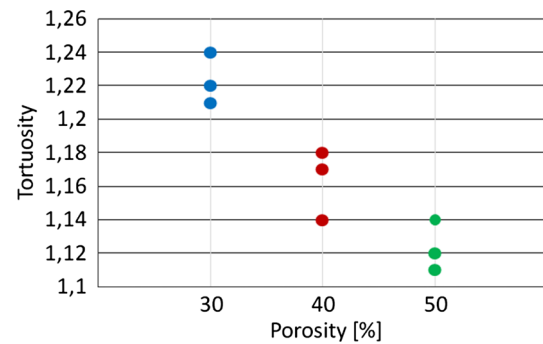
The trend visible in Fig. 8 shows a decrease in tortuosity as the porosity is increased. These results are in good agreement with those presented by Ghassemi et al. [36]. However, a more comprehensive study is required to confirm these results. The results concerning tortuosity in this study are limited, but provide at least an indication of the values of tortuosity for the gas species and the trend over the small range studied here.

Some of the results are compared to experimental work in the literature. However, the experimental studies are conducted on a whole unit cell of an SOFC and therefore some of the results obtained from this numerical study may differ slightly from the experimental results. The maximum ionic current density is compared in the voltage–current density curves found in the literature for the same operating conditions. The ionic current densities obtained from the case studies in this work are slightly higher than several numerical and experimental studies found in the literature for an inlet temperature of 1000 K and operating voltage of 0.7 V. Yang et al. [37] conducted experimental work on an anode-supported SOFC for operating temperatures between 1023 and 1123 K and the current density obtained for 0.7 V was around 6500 A/m^2. However, there are a number of studies that confirm the high ionic current density such as Rogers et al. [38]. They obtained a current density around 13 000 A/m^2 for 1073 K and 0.7 V.

The relatively high ionic current density might be explained by an under-prediction of the overpotential for a small sample of the porous volume which was found by Kanno et al. [10]. Also the high ionic current density is affected by the fact that only the anode is included in this study and not the entire SOFC. The trend and change of the ionic current density due to temperature is supported by Suzue et al. [8] both in magnitude of the maximum ionic current density and the development of the ionic current density in the x-direction. The curve trend can be explained by low ion transport resistance as the porous media in the model is treated as a mixed ionic and electronic conducting

material where the ions and electrons are able to travel through all the solid particles.

By comparing the results with previous results [35] it can be shown that a larger H_2 concentration variation is obtained when the charge transfer, the electrochemical properties and their structural properties are described parallel to each other. This is due to the inter-dependence of the process paths and changes in geometric and kinetic transport properties. The studies in Palabos are compared with standard in-house codes with good agreement.

References

1. Andersson M, Yuan J, Sundén B (2012) SOFC modeling considering electrochemical reactions at the active three phase boundaries. Int J Heat Mass Transf 55:773–788
2. Kakaç S, Pramuanjaroenkij A, Zhou XY (2007) A review of numerical modeling of solid oxide fuel cells. J Hydrog Energy 32:761–786
3. Doraswami U, Shearing P, Droushiotis N, Li K, Brandon NP, Kelsall GH (2011) Modeling the effects of measured anode triple-phase boundary densities on the performance of micro-tubular hollow fiber SOFCs. Solid State Ion 192:494–500
4. Grew KN, Joshi AS, Peracchio AA, Chiu WKS (2010) Pore-scale investigation of mass transport and electrochemistry in a solid oxide fuel cell anode. J Power Sources 195:2331–2345
5. Nam JH, Jeon DH (2006) A comprehensive micro-scale model for transport and reaction in intermediate temperature solid oxide fuel cells. Electrochim Acta 51:3446–3460
6. Joshi AS, Peracchio AA, Grew KN, Chiu WKS (2007) Lattice Boltzmann method for multi-component mass diffusion in complex 2D geometries. J Phys D Appl Phys 40:2961–2971
7. Virkar AV, Chen J, Tanner CW, Kim J (2000) The role of electrode microstructure on activation and concentration polarizations in solid oxide fuel cells. Solid State Ion 131:189–198
8. Suzue Y, Shikazono N, Kasagi N (2008) Micro modeling of solid oxide fuel cell anode based on stochastic reconstruction. J Power Sources 184:52–59
9. Iwai H, Shikazono N, Matsui T, Teshima H, Kishimoto M, Kishida R, Hayashi D, Matsuzaki K, Kanno D, Saito M, Muroyama H, Eguchi K, Kasagi N, Yoshida H (2010) Quantification of SOFC anode microstructure based on dual beam FIB-SEM technique. J Power Sources 195:955–961
10. Kanno D, Shikazono N, Takagi N, Matsuzaki K, Kasagi N (2011) Evaluation of SOFC anode polarization simulation using three-dimensional microstructures reconstructed by FIB tomography. Electrochim Acta 56:4015–4021
11. Dawson SP, Chen S, Doolen GD (1993) Lattice Boltzmann computations for reaction-diffusion equations. J Chem Phys 98:1514–1523
12. Xu Y-S, Zhong Y-J, Huang G-X (2004) Lattice Boltzmann method for diffusion-reaction-transport processes in heterogeneous porous media. Chin Phys Lett 21
13. Aguiar P, Adjiman CS, Brandon NP (2004) Anode-supported intermediate temperature direct internal reforming solid oxide fuel cell I: model-based steady-state performance. J Power Sources 132:113–126
14. Bessler WG, Warnatz J, Goodwin DG (2007) The influence of equilibrium potential on hydrogen oxidation kinetics of SOFC anodes. Solid State Ion 177:3371–3383
15. Newman J, Thomas-Alyea KE (2004) Electrochemical systems, 3rd edn. Wiley-Interscience, Hoboken
16. Nsofor EC, Adebiyi GA (2001) Measurement of the gas-particle heat transfer coefficient in a packed bed for high-temperature energy storage. Exp Therm Fluid Sci 24:1–9
17. Reid RC, Prausnitz JM, Poling BE (1987) The properties of gases and liquids, 4th edn. McGraw Hill, New York
18. Chen S, Dawson SP, Doolen GD, Janecky DR, Lawniczak A (1995) Lattice methods and their applications to reacting systems. Comput Chem Eng 19:617–646
19. Kang QJ, Lichtner PC, Janecky DR (2010) Lattice Boltzmann method for reacting flows in porous media. Adv Appl Math Mech 5:545–563
20. Joshi AS, Grew KN, Izzo JR Jr, Peracchio AA, Chiu WKS (2010) Lattice Boltzmann modeling of three-dimensional, multicomponent mass diffusion in a solid oxide fuel cell anode. ASME J Fuel Cell Sci Technol 7:1–8
21. Kandhai D, Vidal DJ-E, Hoekstra AG, Hoefsloot H, Iedema P, Sloot PMA (1999) Lattice-Boltzmann and finite element simulations of fluid flow in a SMRX static mixer reactor. Int J Numer Methods Fluids 31:1019–1033
22. Geller S, Krafczyk M, Tölke J, Turek S, Hron J (2006) Benchmark computations based on lattice-Boltzmann, finite element and finite volume methods for laminar flows. Comput Fluids 35:888–897
23. Zheng HW, Shu C, Chew YT, Sun JH (2008) Three-dimensional lattice Boltzmann interface capturing method for incompressible flows. Int J Numer Methods Fluids 56:1653–1671
24. Yoshida H, Nagaoka M (2010) Multiple-relaxation-time lattice Boltzmann model for the convection and anisotropic diffusion equation. J Comput Phys 229:7774–7795
25. Breyiannis G, Valougeorgis D (2004) Lattice kinetic simulation in three-dimensional magnet hydrodynamics. Phys Rev E 69:065702
26. Bhatnagar PL, Gross EP, Krook M (1954) A model for collision processes in gases. I. Small amplitude processes in charged and neutral one-component systems. Phys Rev 94:511–525
27. Shan X, Doolen G (1996) Diffusion in a multicomponent lattice Boltzmann equation model. Phys Rev E 54:3614–3620
28. Huber C, Parmigiani A, Chopard B, Manga M, Bachmann O (2008) Lattice Boltzmann model for melting with natural convection. Int J Heat Fluid Flow 29:1469–1480
29. Kang Q, Litchner PC, Zhang D (2007) An improved lattice Boltzmann model for multicomponent reactive transport in porous media at the pore scale. Water Resour Res 43:W12S14
30. Chiu WKS, Joshi AS, Grew KN (2009) Lattice Boltzmann model for multi-component mass transfer in a solid oxide fuel cell anode with heterogeneous internal reformation and chemistry. Eur Phys J Spec Top 171:159–165
31. Latt J (2007) Hydrodynamic limit of the lattice Boltzmann equations. PhD Thesis, University of Geneva
32. Wolf-Gladrow DA (2000) Lattice-gas cellular automata and lattice Boltzmann models. An introduction. Springer, Berlin
33. Dardis O, McCloskey J (1998) Lattice Boltzmann scheme with real numbered solid density for the simulation of flow in porous media. Phys Rev E 57:4834–4837
34. He X, Li N (2000) Lattice Boltzmann simulation of electrochemical systems. Comput Phys Commun 129:158–166
35. Paradis H, Sundén B (2012) Evaluation of lattice Boltzmann method for reaction-diffusion process in a porous SOFC anode microstructure. In: Proceedings of the ASME 2012 10th

international conference on nanochannels, microchannels and minichannels, ICNMM2012-73163, Puerto Rico, USA

36. Ghassemi A, Pak A (2011) Pore scale study of permeability and tortuosity for flow through particulate media using lattice Boltzmann method. Int J Numer Anal Methods Geomech 35:886–901

37. Yang S, Chen T, Wang Y, Peng Z, Wang WG (2013) Electrochemical analysis of an anode-supported SOFC. Int J Electrochem Sci 8:2330–2344

38. Rogers WA, Gemmen RS, Johnson C, Prinkey M, Shahnam M (2003) Validation and application of a CFD based model for solid oxide fuel cells and stacks. ASME J Fuel Cell Sci Technol 1762:517–520